

See discussions, stats, and author profiles for this publication at: <https://www.researchgate.net/publication/13605532>

# Texture Evolution during the Polydomain-Monodomain Transition in Nematic Elastomers

ARTICLE *in* MACROMOLECULES · AUGUST 1998

Impact Factor: 5.8 · DOI: 10.1021/ma980195j · Source: PubMed

---

CITATIONS

63

---

READS

33

4 AUTHORS, INCLUDING:



**Stuart Clarke**

University of Cambridge

**131** PUBLICATIONS **1,857** CITATIONS

SEE PROFILE



**Eugene M Terentjev**

University of Cambridge

**304** PUBLICATIONS **7,445** CITATIONS

SEE PROFILE

# Texture Evolution during the Polydomain-Monodomain Transition in Nematic Elastomers

S. M. Clarke and E. M. Terentjev\*

*Cavendish Laboratory, University of Cambridge, Madingley Road, Cambridge CB3 0HE, U.K.*

I. Kundler and H. Finkelmann

*Institut für Makromolekulare Chemie, Universität Freiburg, Sonnenstrasse 5, D-79104 Freiburg, Germany*

*Received February 9, 1998; Revised Manuscript Received May 15, 1998*

**ABSTRACT:** We have studied the behavior of a liquid crystalline elastomer undergoing a polydomain–monodomain transition. The textures emerging under increasing extensional load have been examined with a combination of optical microscopy, X-ray, and small-angle polarized light scattering. The experimental data are interpreted in terms of reorientation of the local director with increasing extension. The results of this combination of techniques at low extensions are consistent with a two-dimensionally periodic director texture. The amplitude of this modulation decreases continuously as the mesogens are pulled into the extensional direction at high loads. In this manner the samples which are polydomain under no load become essentially monodomain with increasing extension.

## 1. Introduction

Liquid crystalline elastomers, LCE, are weakly cross-linked percolating networks of polymer chains with mesogenic groups either incorporated in the polymer backbone or as side groups. The materials used in this work consist of cross-linked siloxane polymer backbones with mesogenic side groups. There are a number of chemical moieties that can be used to permanently cross-link the network of polymer chains including flexible cross-links, varying in functionality and their own mesogenic properties. An important parameter in determining the characteristics of the elastomers is the cross-link density. Below about 5% the materials are usually liquidlike with properties similar to those of polymer melts. For cross-link densities above 20% they are essentially rigid and glassy (i.e. nonrubbery). The interest in these new materials arises from the competition of liquid crystalline order of the mesogens, e.g., nematic or smectic, and the elastic properties of the underlying polymer network. A wide variety of behavior is possible depending upon the method of preparation, temperature, and applied stress.<sup>1,2</sup>

A number of physical techniques have been used to characterize these materials including stress–strain measurements, X-ray diffraction, and IR measurements in an attempt to relate the behavior of the mesogens, on molecular and mesoscopic scales, to external fields,<sup>3–7</sup> in particular, extensional stress. In some cases optical microscopy has been used to examine the morphology of the elastomers. However, the length scales of textures, typically in the micrometer range, are often too small for reliable interpretation by optical microscopy. Light scattering on the other hand is ideally suited to the investigation of structural features on this length scale. Additionally, light scattering is sensitive to correlations in the sample which may not be evident in a real space image.<sup>8</sup>

Since their discovery in the early 1980s, liquid crystalline elastomers have been observed to possess a characteristic polydomain texture with variations of the

nematic director on a length scale similar to the wavelength of light, making the materials optically opaque. This texture appears to be a universal feature of elastomers, whether nematic or smectic, of all chemical compositions studied. Such behavior may be related to the characteristic Schlieren texture of liquid crystal polymer melts.<sup>9</sup> However, unlike melts where the texture shows a coarsening behavior when the material approaches the equilibrium state, the cross-linked networks seem to have the polydomain texture as the equilibrium state.<sup>6,7</sup> This paper examines structural transformations during the polydomain to monodomain transition in LCE (which we shall refer to as the P–M transition).

The liquid crystalline behavior of mesogenic polymers only occurs over a restricted temperature range with an upper limit set by the nematic–isotropic transition temperature  $T_{ni}$  and a lower limit set by the crystal–nematic or glass transition. At this point it is important to specify the definition of the nematic order parameter in more detail. Polydomain textures with small-scale variation of the nematic director  $\mathbf{n}(\mathbf{r})$  have to be characterized by two different parameters, depending upon the length scale. The existence of a liquid crystalline order is manifested by alignment of mesogenic groups, correlated within a characteristic coherence length  $\xi_N$  which, in nematics, is on the order of 100 Å, much smaller than the wavelength of light. A tensor nematic order parameter is established by thermodynamic averaging over this correlation volume

$$Q_{\alpha\beta} = \frac{3}{2} \langle u_\alpha u_\beta \rangle - \frac{1}{2} \delta_{\alpha\beta} = Q(T) \left[ n_\alpha n_\beta - \frac{1}{3} \delta_{\alpha\beta} \right] \quad (1)$$

with the unit vector  $\mathbf{u}$  specifying the long axes of mesogenic molecules. The principal axis of this order parameter, the director  $\mathbf{n}(\mathbf{r})$ , may wander in space with another characteristic length scale,  $\xi_D$ , the “domain size” of the texture. One can average the direction of  $\mathbf{n}(\mathbf{r})$  over the whole sample, thereby measuring the deviation

of  $\mathbf{n}(\mathbf{r})$  from some globally defined axis, for example, the direction of mechanical stress. When such deviation is parametrized by a single angle,  $\beta(\mathbf{r})$ , the resulting mean orientation parameter should be defined as  $S = [\frac{3}{2}\langle \cos^2 \beta(\mathbf{r}) \rangle - \frac{1}{2}]Q(T)$ . Here we assign different names to these order parameters: a nematic order parameter  $Q_{\alpha\beta}$  (with  $Q(T) \neq 0$  the material is nematic and locally birefringent) and the mean orientation parameter  $S$  (with  $S \neq 0$  there is a correlation in director orientation  $\mathbf{n}(\mathbf{r})$  in different sample regions); the maximal value of  $S = Q$  describes a fully monodomain sample.

X-ray scattering from liquid crystalline materials has been used extensively to determine structural features, including the order parameter. Polydomain nematic samples with no preferred orientation ( $S = 0$ ;  $Q \neq 0$ ) show scattering patterns with a pronounced ring that has a uniform azimuthal intensity distribution. When the material is well aligned along a single direction, then the ring of scattering shows a very nonuniform azimuthal intensity distribution. An estimate of the mean orientational order parameter,  $S$ , can be obtained from the distribution of the intensity of scattering around this ring as described by refs 10–12. Unless the form-factor of individual mesogens is known very reliably, these methods only give an estimate of the single mesogen distribution function.<sup>11</sup> However, this usually provides a satisfactory approximation for  $S$ .

Polarized light scattering probes the local contrast in refractive indices, essentially the degree of misorientation of nematic domains in a texture. In this work we examine the structural changes occurring in polydomain nematic elastomers subjected to an extensional stress which, after a certain transitional region, results in a macroscopically aligned “monodomain” sample. There are many indications that topological defects, essentially the “fossil” domain walls, remain in such a state.<sup>13</sup> This “monodomain” is thermodynamically unstable and returns to its original texture after removal of the stress. In contrast, a sample prepared as an equilibrium monodomain retains its orientational order in the absence of stress.

The main motivation for this paper is to identify, characterize, and interpret the features of scattering patterns of a randomly disordered birefringent medium and its evolution during the P–M transition. An outline of the scattering theory is presented in the Appendix. After the experimental methods are detailed, the results of light scattering, stress–strain, and X-ray measurements will be given and interpreted in terms of a simple model of the orientation of mesogenic groups. The structural information obtained from the light scattering experiments is related to the observed stress–strain behavior and to the nematic order parameter,  $Q$ , obtained from X-ray measurements. A proposed model of the director orientation distribution, accounting for the observable light scattering patterns in different configurations, can also be used to calculate the real space image that would be visible through an optical microscope provided the length scale is suitable and the sample transmits enough light. In reality, the characteristic length of 2–3  $\mu\text{m}$  and the high degree of disorder in the samples make such observation difficult (which is the main motivation for using the light scattering techniques). However, the principal elements of texture predicted by the model can be identified in the microscopic images.

**Polarized Light Scattering.** Light scattering has been used to study polymer morphology for some time and excellent reviews are available.<sup>14</sup> In particular there have been several investigations of the scattering of polarized light to characterize polymer spherulite morphology and the behavior of liquid crystalline materials.<sup>9</sup>

Light scattering by nematic liquid crystals results from variations in orientation of the director field  $\mathbf{n}(\mathbf{r})$  of the mesogens. In this work, which considers scattering from thin samples, it is assumed that the director is confined to the sample plane. The plane polarized light is incident normal to the sample plane. The local orientation of the optical axis with respect to the plane of polarization of the incident light is given by the angle  $\beta(\mathbf{r})$ . The sample is considered as an array of domains each of which scatters the incident light with a certain amplitude which depends on  $\beta$ . The scattering from each mesogen or element of the sample adds coherently with an appropriate phase term depending upon their relative spatial distribution. This phase term is of the form  $\exp(i\mathbf{q}\cdot\mathbf{r})$ , where  $\mathbf{r}$  is the position in the plane of the sample and  $\mathbf{q}$  is the scattering vector with the modulus  $|\mathbf{q}| = 4\pi(\sin \theta)/\lambda$ , where  $\theta$  is half the scattering angle and  $\lambda$  is the wavelength of the light. The observed intensity is the square of the sum of amplitudes of scattering from each element of the sample. In this manner the scattering from the sample can be calculated from a model giving the spatial and orientational distribution of the director  $\mathbf{n}(\mathbf{r})$ .

When the sample is placed between a polarizer and analyzer pair, only the light that is transmitted by the analyzer after the scattering process will be detected. The amplitude of this light depends on the relative orientation of the incident light field, the local director  $\mathbf{n}(\mathbf{r})$ , and the polars. The plane-polarized incident electric field interacts with each mesogenic group producing two components of scattered light, one parallel to the incident light polarization and another normal to the incident beam polarization. Under crossed and parallel polars, denoted HV and VV respectively, the amplitude scattered by each sample element is of the form (cf. the Appendix)

$$A_{\text{HV}} = \Delta \sin(2\beta); \quad A_{\text{VV}} = \Delta \cos^2(\beta) - B_t \quad (2)$$

Here  $\Delta$ , the birefringence, is the difference in refractive index along the director ( $m_{\parallel}$ ) and perpendicular to it ( $m_{\perp}$ ), and  $\beta$  is the angle between the local optical axis and the polarizer.  $B_t$  is the difference in refractive index along the mesogen axis,  $m_{\parallel}$ , and that of the surroundings,  $m_s$ .<sup>14,15</sup> These simple forms of  $A_{\text{HV}}$  and  $A_{\text{VV}}$  are obtained for small angle scattering in both the Rayleigh–Gans–Debye (RDG) and anomalous diffraction (AD) approximations for the director confined to two dimensions, under the particular conditions outlined in the Appendix. It should be noted that RDG and AD approximations do not always give the same result, notably in the case of a homogeneous spherical particle.<sup>16,17</sup>

The equation for  $A_{\text{HV}}$  indicates that, under crossed polars (HV), regions of the nematic director oriented parallel to the polars, i.e.,  $\beta = 0$  or  $90^\circ$ , do not contribute to the scattering pattern while the regions oriented at  $\beta = 45^\circ$  contribute the most. Under parallel polars (VV) the scattering is more complex, arising from the birefringence of each scattering element but also from the

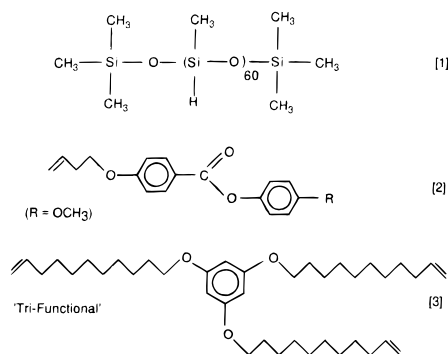


**Figure 1.** Details of the materials used in the preparation of the liquid crystal elastomer.

contrast with the surroundings.<sup>14</sup> The strongest angular variation in this case is contained in the  $\Delta \cos^2(\beta)$  term in  $A_{VV}$  which has its maximum when the local director is oriented parallel or perpendicular to the polars. Additionally, under parallel polars the unscattered laser beam is also allowed to pass and will be detected. This is not the case with crossed polars where the unscattered laser beam should be extinguished, if the polars are 100% efficient.

## 2. Experimental Section

**2.1. Elastomer Synthesis.** Details of the synthesis of the siloxane-based liquid crystalline elastomers have been described elsewhere.<sup>3,18</sup> The component molecules are given in Figure 1. The siloxane polymer backbones "1" were substituted with mesogenic side-groups "2" to form a side-chain nematic polymer. Prepolymers of approximately 60–70 repeat units have been cross-linked with flexible trifunctional cross-links "3" with an estimated density of 7.5%. The DSC measurement indicates a glass transition at  $T_g = -5$  °C, very close to the  $T_g$  of corresponding polymer melt, and the clearing point (the nematic–isotropic transition) at  $T_{ni} = 41$  °C. During the synthesis a certain amount of residual compounds have been left in the system and play the role of isotropic solvent slightly swelling the network and making the mechanical relaxation faster. However, since we are examining the equilibrium structure of the elastomer, the effect of this small quantity of solvent is taken to be minor. A separate publication will present a detailed comparative study of a range of elastomer samples, with and without solvent, with flexible trifunctional and rigid-rod bifunctional cross-links of varying concentrations. As indicated in the Introduction, this paper focuses on the interpretation of the characteristic light scattering images, which appear to be universal across all types of studied polydomain elastomers.

**2.2. Light Scattering.** The experimental light scattering configuration employed here is similar to previous light scattering work<sup>19,20</sup> where a horizontal sample was probed by a vertical laser beam. In this present work it has been necessary to suspend the samples vertically to avoid the freely suspended sample being deformed by gravity, and so the incident laser beam is horizontal. Light with a wavelength of 488 nm and intensity cross-section corresponding to  $TEM_{00}$  emitted by an argon ion laser is collimated to form a parallel beam and spatially filtered before falling on a diaphragm placed immediately before the sample position. Light scattered by the sample is collected by a large diameter, short focal length lens placed as close to the sample as possible. This lens, with focal length,  $f$ , projects the scattering pattern from the sample onto a diffusing screen. This screen is placed at distance equal to  $f$  away from the lens where the scattering pattern from the sample is focused. The lens is placed close to the sample to optimize the accessible range of scattering angles. The scattering pattern on the diffusing screen is projected onto the sensitive surface of a charged coupled device

(CCD) by means of a further lens system attached to the CCD camera. The CCD device enables the rapid collection of quantitative intensity data for subsequent data analysis as described previously.<sup>20</sup> Data were collected on a computer and subsequently subjected to detailed analysis. The intensity and scattering angles can be calibrated with precision diffraction gratings. A polarizer (diameter 40 mm) and analyzer (diameter 150 mm) were placed immediately before and after the sample position. The polaroid material<sup>21</sup> had an extinction ratio of 0.0005% or  $5 \times 10^{-6}$ . Both the polarizer and analyzer could be rotated independently by 360°.

The sample was suspended from a sensitive stress gauge and could be extended either by a micrometer, in a controlled strain regime, by a motor with a controlled strain rate, or by the application of weights in a controlled stress regime. The whole sample, stress gauge, and extensional apparatus is contained in a thermostatically controlled box with glass windows. Both the small entrance window (20 × 70 mm) and the large exit window (120 × 120 mm) have flexible seals and adjustment devices that allow them to be tilted to remove unwanted reflections. The whole assembly is mounted on translation stages to allow any portion of the sample to be probed with the laser. The stress measuring device<sup>21</sup> gave data in arbitrary units which were converted to newtons after calibration with weights at each temperature investigated. The thermostatic control<sup>21</sup> gave an experimental temperature stability of less than 1°.

**2.3. X-ray Measurements.** X-ray measurements were performed in pinhole geometry with a flat-plate detector at the Material Science Department, University of Cambridge. A static copper anode without filter or monochromator running at 25 mA and 40 KV was used. Count times were 1 h. The images on the developed photographic films were scanned using a back-illuminated scanner designed for the scanning of negatives. No intensity calibrations were performed. The sample was supported by the same stress gauge used in the light scattering experiments and was extended in controlled strain mode with a micrometer pitch screw and captive nut mechanism.

**2.4. Stress–Strain Measurements.** Stress–strain measurements were obtained from samples during light scattering and X-ray investigations. The thin samples used in this work were cut to two shapes: a rectangle or a "prenecked" shape used previously by other workers<sup>22</sup> to prevent the sample tearing at the clamped ends. Although the stress in such a precut sample is concentrated in the central region, both shapes of sample behaved in a similar manner. As expected, the prenecked samples could be stretched to a far greater extent, allowing a wider region of stress to be explored. The samples were annealed at temperatures above their  $T_{ni}$  and cooled slowly before the measurements were begun. During the scattering studies the relaxation was monitored by following the changing stress with time. At high temperatures, close to  $T_{ni}$ , the relaxation was very fast. At lower temperatures it was much slower and in some cases took days to relax completely. In these cases the samples were extended at a slow, controlled strain rate to allow data to be collected in a reasonable time. Stress values are calculated from the experimentally determined load and measured sample dimensions and are presented as nominal stress. The strain,  $\epsilon$ , is defined here as the total change in length of the sample,  $\Delta L$ , divided by the unstretched length,  $L_0$  (i.e.  $\epsilon = [L - L_0]/L_0$ ), although strictly a more complicated calculation is needed for a "prenecked" sample where the initial deformation mainly occurs in the middle of the sample.

**2.5. Optical Microscopy.** Selected samples extended in controlled strain fashion were examined by optical microscopy with a Zeiss Axioplan Microscope. These samples could be viewed in real space under crossed polars. The microscope has been equipped with the DIC (differential interference contrast) utility that enhances a weak contrast and also adds a color scheme to the different textures. The effective scattering image could also be formed by insertion of a Bertrand lens. A calibrated scale bar was used to obtain the dimensions of features in the real space patterns, and gratings were used



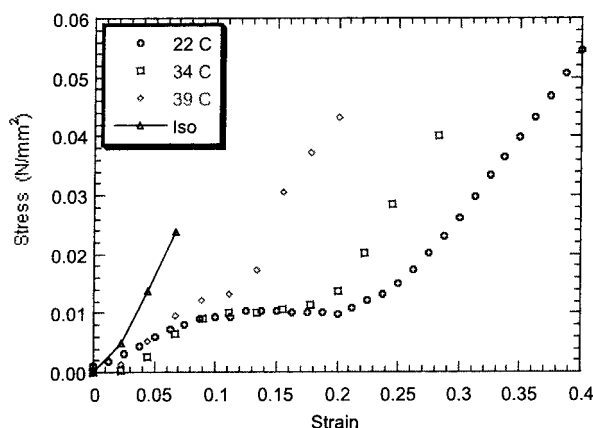


**Figure 2.** Stress–strain plots for polydomain nematic elastomer at temperatures of 22, 34 and 39 °C. The connected data points show the stress–strain plot for the isotropic elastomer.

to calibrate the scattering patterns. The sample could be illuminated either by white light or light monochromated with filters. All optical microscope measurements were made at room temperature.

### 3. Results

**3.1. Stress–Strain Curves.** The experimentally determined stress–strain curves for the nematic elastomer at temperatures of 22, 34 and 39 °C and in the isotropic phase above the transition temperature  $T_{ni}$  are given in Figure 2. These curves exhibit the general trend observed with other elastomers reported previously<sup>6</sup> with an initial rise in stress and then a plateau region where the transition to the transparent “monodomain” sample begins, before a further rise in stress in an optically aligned sample occurs. The plateau values of the stress are of a similar order to those reported earlier. These features are evident at all the temperatures investigated, with the plateau stress apparently independent of temperature and approximately equal to  $10^{-2}$  N/mm<sup>2</sup>. The principal difference between the elastomer mechanical response at different temperatures is the extension at the end of the plateau, which falls with increasing temperature. We refer to the region in the stress–strain curves after the plateau as the “monodomain” region.

**3.2. Optical Microscopy.** Real space images of the elastomer, obtained in the region of polydomain–

monodomain transition, are poorly resolved in the optical microscope because the main texture features are occurring on the small length scale 2–3  $\mu$ m. However, a sketch is given in Figure 3a to represent the texture that is typically observed. The sample was illuminated with white light and held between crossed polars. The orientation of the polars is horizontal and vertical in the picture, i.e., parallel and perpendicular to the extension axis. This drawing indicates the characteristic texture seen in a large proportion of the sample, an aligned periodic rectangular array of intensity minima separated by bright regions, systematically colored in alternating pink and green if viewed in white light. The color scheme, introduced by the DIC phase contrast, allows the differentiation between two opposite director orientations at 45° to the polars.

**3.3. Light Scattering.** Light scattering patterns obtained from the nematic elastomer undergoing the P–M transition are given in Figure 4. These patterns have been obtained from the sample under an extension  $\epsilon = 0.25$  at a temperature of 22 °C, at a point corresponding to the end of plateau region of the stress–strain curve in Figure 2 where the peak features are most clearly visible. The two patterns were taken under crossed polars (HV), either parallel to the extension axis (HV<sub>0</sub> configuration, Figure 4a) or at 45° to the extension axis (HV<sub>45</sub> configuration, Figure 4b). The center of the pattern corresponds to the position where the unperturbed straight-through beam would be if not removed by the crossed polars. The extensional direction of the elastomer is indicated in Figure 3a.

There is a characteristic form to the HV<sub>0</sub> pattern containing two intense elongated, “narrow” peaks, describing the length scale in the direction perpendicular to the stress axis, and two “broad” less intense peaks that correspond to the texture features in the direction along the stress. There is also a minima at low  $q$ . These patterns agree well with the reciprocal space images obtained in the polarizing microscope with a Bertrand lens (not shown).

We have characterized these peaks in some detail. On tilting the sample in two perpendicular directions it is found that the two intense “narrow” peaks do not significantly change in intensity. However the two “broad” peaks are rapidly reducing in intensity, when not viewed at 90° to the sample. We therefore propose that the three-dimensional reciprocal space image from

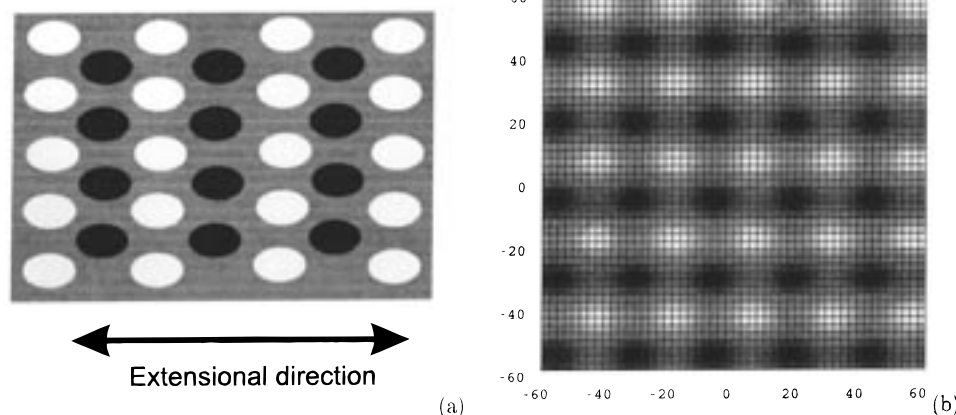


**Figure 3.** (a) Sketch representing the characteristic optical microscope images of the liquid crystal elastomer under crossed polars at the smallest extension where there is appreciable transmission, HV<sub>0</sub> configuration. The arrow indicates the direction of the sample extension. (b) Calculated real space image for the additive two-dimensional sinusoidal director modulation discussed in the text, also in the HV<sub>0</sub> configuration.

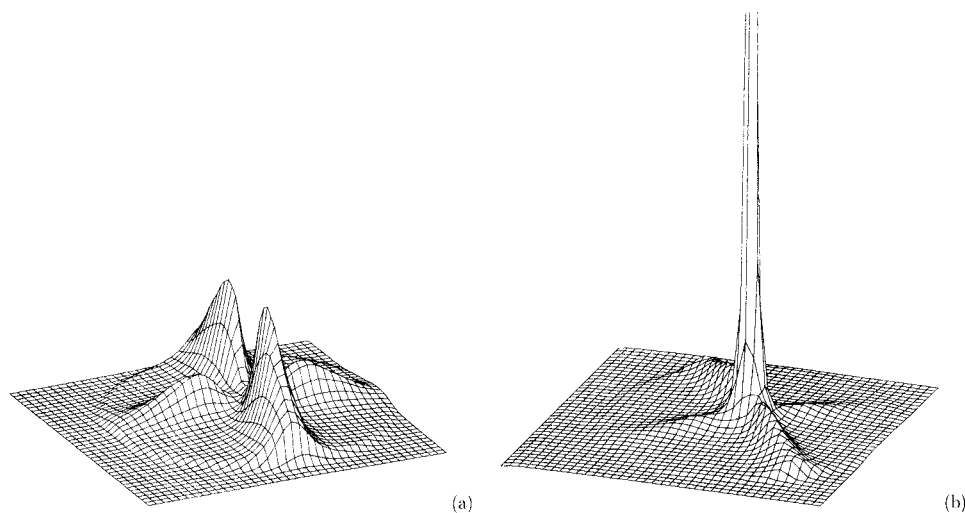


**Figure 4.** Light scattering patterns at a temperature of 22 °C with an imposed strain  $\epsilon = 0.25$ : (a) under crossed polars with the extensional direction of the elastomer parallel to the polaroid and perpendicular to the analyzer, HV<sub>0</sub>; (b) under crossed polars at 45 degrees to the direction of extension, HV<sub>45</sub>. (Filters have produced a linear intensity scale, which is approximately the same for both figures.)

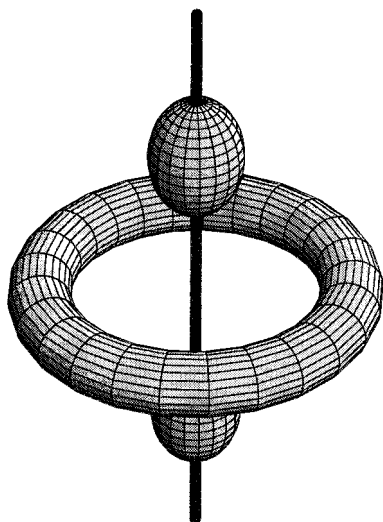


**Figure 5.** Schematic illustration of the three-dimensional distribution of light scattering intensity during the P–M transition. The line drawn on the vertical axis indicates the direction of sample extension.

this sample is in fact a torus of intensity in the plane normal to the extensional axis (making the “narrow” peaks) and two localized maxima on the extensional axis above and below the torus (“broad” peaks) as schematically illustrated in Figure 5. The observed patterns are two-dimensional sections through this full three-dimensional scattering. However, only a small tilting of the sample was possible due to space restrictions in the sample environment and problems with transmission. There are, therefore, significant uncertainties in this conjecture, although the conclusion of cylindrical symmetry about the extensional axis implicit in this hypothesis is not unreasonable. We have been unable to observe any higher order reflections in this configuration.

Experimentally determined peak positions at temperatures of 22 and 34 °C are given in Table 1. The positions of the reflections correspond to a  $|q|$  of  $2.8 \mu\text{m}^{-1}$  at 22 °C and  $2.5 \mu\text{m}^{-1}$  at 34 °C, which is equivalent to  $d$  spacings of 2.2 and  $2.5 \mu\text{m}$ , respectively. Most

**Table 1.** The summary of scattering data at different temperatures<sup>a</sup>

temperature (°C)	narrow peak ( $q, \mu\text{m}^{-1}$ )	broad peak ( $q, \mu\text{m}^{-1}$ )
22	2.8	2.8
34	2.5	2.5
cooling	0–2.5	0–2.5

<sup>a</sup> “Cooling” in the temperature column denotes the process of bringing the sample down from isotropic phase (above  $T_{\text{ni}} = 41$  °C) to approximately 34 °C. The corresponding entries in peak position columns show the range of peak movement. This experimental error in peak position is estimated as  $\pm 0.2 \mu\text{m}$ , and the two sets of data points in Figure 6a coincide within the error.

importantly, the positions of both types of reflection are insensitive to extension, remaining essentially unchanged in position over the measurable range of sample deformations. At 34 °C, for an extension of 14%, the peaks shift in the extensional direction by only 1%. At 22 °C, for an extension of 16%, the peaks move by only 2%. Under increasing strain, the spacing in the extensional direction might be expected to increase, corresponding to a movement of peaks to lower  $q$ , while the peaks normal to the extensional direction might be expected to move in the opposite direction to conserve volume of the sample. The experimental resolution ( $\pm 1$  pixel) results for the narrow peaks in an error on the order of 5%; the maxima of the broad peaks are harder to locate, and the error in the peak position is estimated to be approximately 10%. So we conclude that no change in characteristic texture dimensions has occurred under extension.

The shift in position with increasing temperature was investigated further by heating the sample to the isotropic state, above 40 °C, and then collecting patterns as the sample cooled back to the nematic phase at 34 °C. During this heating cycle the sample was given a constant load equivalent to a position well into the aligned region in the stress–strain curve. The variation in peak positions with temperature are given in Figure 6 and listed in Table 1. In particular, Figure 6a illustrates the pronounced movement of the peaks which appear out of the straight-through beam direction and move to higher angles with decreasing temperature. These results, unexpectedly, indicate that the macro-

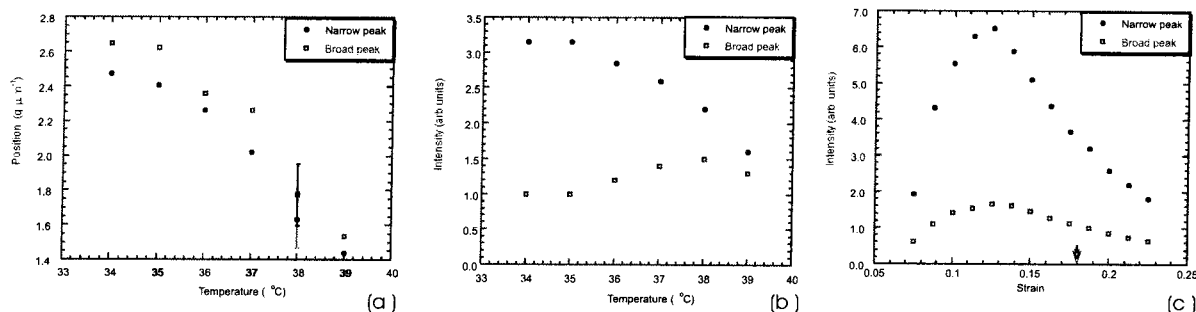


**Figure 6.** Variation with temperature of peak positions, plot a, and peak intensities, plot b, on cooling the sample from the isotropic phase to 34  $^{\circ}C$ . Variation of narrow peak intensity with increasing extension at a temperature of 34  $^{\circ}C$ , plot c. The error bars in plot a indicate the uncertainty in the peak position. The arrow in plot c indicates the value of strain ( $\epsilon = 0.18$ ), under which plots a and b were obtained.

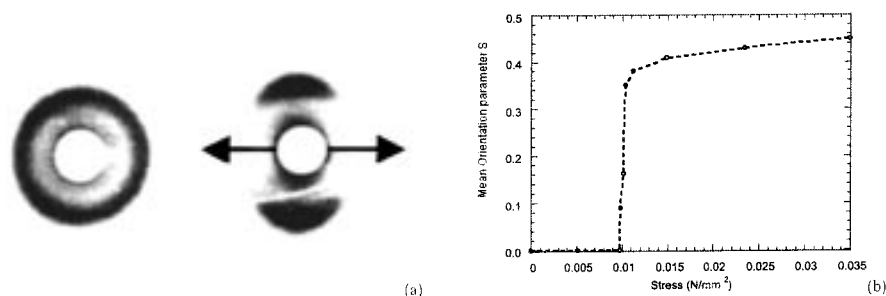


**Figure 7.** (a) X-ray scattering patterns from the nematic elastomer before,  $\epsilon = 0$ , and after the P–M transition,  $\epsilon = 0.35$ , at a temperature of 22  $^{\circ}C$ . The arrow on the second image marks the direction of the elastomer extension. (b) Mean orientation parameter  $S$  as a function of stress for the same sample, obtained from the analysis of X-ray images.

scopic orientational correlations in the sample increase in length as  $T_{ni}$  is approached from below.

The intensities of the narrow and broad peaks on cooling the sample from the isotropic region to 34  $^{\circ}C$  are given in Figure 6b. This plot shows that the intensity of the narrow peaks increases with falling temperature. Initially the broad peak intensity also increases in a similar fashion but stops growing while the narrow peak keeps increasing.

Finally, Figure 6c presents the variation of intensity of the two peaks evident in the  $HV_0$  configuration as a function of extension. At low extension the sample is opaque due to strong multiple scattering. When the samples are stretched into the P–M transition (the plateau stress region), they become more transparent and there is an initial increase in intensity of these peaks, which we attribute to the increase in transmission. This is followed by a loss of intensity with continuing extension. It is to be noted that there are still significant changes in the scattering well beyond the end of the plateau in stress (which at this temperature ends at  $\epsilon \sim 0.18$ ). The intensities of all the peaks diminish with increasing strain, however the narrow peaks disappear more quickly while remaining more intense than the broad peaks.

The intensity of both types of peaks fall significantly on rotation of the crossed polars with respect to the sample, from a maximum in the  $HV_0$  configuration to a minimum in the  $HV_{45}$  configuration, where only a residual “shoulder” remains of the pronounced peaks in  $HV_0$ . It is clear that the observed scattering patterns are intimately linked to the director texture in the sample and the direction of the applied stress; there is no cylindrical symmetry about the axis of incident light. This is in contrast with earlier observations of four-peak

scattering patterns in liquid crystalline polymers,<sup>9</sup> apparently determined by the orientation of polars.

The most pronounced feature of the scattering pattern obtained in the  $HV_{45}$  alignment is the very intense maximum at low  $q$ , decaying monotonically with increasing scattering angle. This peak is also quite narrow, giving a very simple scattering pattern. This feature suggests that a large proportion of the mesogens (or, more correctly, domains of locally uniform director) are aligned at 45 $^{\circ}$  to the polars in this configuration, i.e., in the extensional direction. As discussed above, the four peaks evident in the  $HV_0$  configuration have essentially disappeared.

Similar light scattering measurements were taken when the samples were extended under controlled stress. The scattering patterns at the various stress values agreed well with those obtained at the same stress value under controlled strain.

**3.4. X-ray Scattering.** Figure 7 presents the X-ray scattering patterns from the nematic elastomer at room temperature at strains of zero and  $\epsilon = 0.35$  (a), the latter point corresponding to the stress–strain curve of Figure 4 well into the aligned region. The ring of intensity is at the scattering angle of 20 $^{\circ}$ . A significant increase in mean orientational order  $S$  of the local nematic director is indicated by the azimuthal redistribution of intensity around the pronounced scattering ring. The parameter  $S$  has been estimated from these data and is presented in Figure 7b as a function of stress. It is clear from this figure that there is a marked jump in the order parameter at the plateau stress with only much smaller variations above and below this stress value. This behavior agrees well with earlier reported observations with closely related materials<sup>6,23,24</sup> and with the expectations of a recent theoretical model.<sup>13</sup>



#### 4. Discussion

In this section we propose to indicate how the observed scattering patterns and optical microscopy images can be interpreted in terms of a simple model of director orientation and its evolution under stress.

**4.1. Model Calculations.** In order to determine the scattering from a model distribution of the director,  $\mathbf{n}(\mathbf{r})$ , each element is taken to scatter with an amplitude depending upon its orientation relative to the polarizer and analyzer and a phase term depending upon the location of that sample element relative to its neighbors. This simple construction has been used to model the scattering from a number of different arrays of birefringent elements including polymer spherulites,<sup>25</sup> liquid crystal mesogens in partially oriented domains with a rodlike shape,<sup>15,26</sup> and isolated disclinations in liquid crystals.<sup>9</sup> A model describing a one-dimensional sinusoidal or "zigzag" variation in the director orientation has been used to explain the "banding" in a number of polymer systems.<sup>27</sup>

Calculations of the scattering that arises from spherulites and isolated disclinations are not consistent with the experimental scattering from the LCEs reported here. The distributions of birefringent elements in polymer spherulites and isolated disclinations with strength  $\pm 1/2$  are cylindrically symmetric and are calculated to give patterns that are linked to the orientation of polars and remain unchanged on rotation of the sample. The features in the scattering patterns given here are clearly fixed with respect to the sample and have an intensity that does depend on the orientation of the sample with respect to the polars. Isolated disclinations of the type  $S = \pm 1/2$  are calculated to give HV and VV patterns with only two maxima, while the experimental patterns reported here have four peaks. If a sample contains disclinations randomly positioned and oriented, these two spots become a ring of intensity. Both of these models, single oriented disclinations and randomly oriented disclinations, do not recreate the four-peak patterns presented here, in Figure 4.

The calculated scattering from models including interference between disclinations has also been considered.<sup>9</sup> Interference can give rise to peaks where the peak positions are attributed to a characteristic distance between disclinations. The separation between disclinations was reported to increase with time as pairs of disclination were annihilated and the texture coarsened. This coarsening was manifested by the scattering peak position moving toward small angles. More complex changes in the scattering patterns have been observed arising from the arrangement of disclinations when the samples were sheared.<sup>28</sup> In this present work no evidence of disclinations was found under the optical microscope, and the scattering patterns in HV and VV configurations do not agree with the calculated images based on this model.

The theory for scattering by a partially aligned distribution of long rodlike domains each containing mesogens oriented at some angle to the rod axis has been considered by ref 15 and used to explain the experimental scattering observed with PTFE and HPC polymers.<sup>26</sup> The original theoretical paper considered an elliptical distribution of rod orientations and also included reorientation of the mesogens within the rods at high alignment. The intensity of scattering has then been calculated under parallel (VV) and crossed (HV) polars configurations. The rods were considered to be

very long compared to their width and the scattering was considered to be the incoherent sum of scattering intensities from each rod. A range of scattering patterns under crossed and parallel polars were determined, depending upon the value of parameters used in the calculations. In all cases the scattering patterns fall in intensity from the maxima at  $q = 0$  under both parallel and crossed polars. The experimental HV<sub>0</sub> patterns presented here in Figure 4a clearly exhibit a minimum at low angles in disagreement with this model of rodlike objects. Another approach to calculating the scattering from polymeric materials has been the approach of Debye and Bueche, modified by Stein,<sup>29</sup> which considers the scattering to arise from fluctuations in density, birefringence, and orientational correlations in the sample. Calculations based on simple correlation functions of the form  $\exp(-r/\xi)$  and  $\exp(-r^2/\xi^2)$  predict cylindrical symmetry to the scattering and a maxima at low  $q$  for the HV<sub>0</sub> scattering patterns, again in disagreement with our experimental data.

We conclude that these simple models do not account for the experimentally observed scattering from LCE presented in this work.

**4.2. Two-Dimensional Director Modulation.** Several of the key characteristics observed in the scattering from LCEs presented here are observed in the scattering from "banded" textures in polymers.<sup>27,30,31</sup> These polymers are characterized by a director field that varies in one-dimension in a sinusoidal fashion of the form  $\beta \approx C \sin(x/a)$ . This form of the director field modulation is referred to as the "divergence" function.<sup>27</sup> According to this model, the sample in real space exhibits a "banding" texture with stripes across the sample. The scattering from such a model can be calculated. The scattering patterns under crossed polars consist of a series of spots perpendicular to the stripes, in much the same manner as a diffraction grating.<sup>32</sup> The relative intensity of the spots depends on the orientation of the polars with respect to the sample and the amplitude of the divergence function. If the polars are parallel/perpendicular to the stripes then there are no peaks at zero  $q$  and no even-indexed reflections although the odd-order reflections are strong. If the polars are oriented at 45° to the stripes, then there is strong intensity of scattering at zero  $q$  and for even reflections, while the odd-order reflections are weak or absent. Calculations based on this model have been used to distinguish functions that vary sinusoidally or vary in a "zigzag" fashion. The appearance and behavior of the intensity maxima and the low intensity at zero angles in certain orientations are in good agreement with the results presented here. However, the experimental patterns presented here include two sets of reflections orthogonal to one another rather than just one set predicted by the one-dimensional divergence function model.

This previous work using a one-dimensional modulation model can be generalized to two dimensions in the simplest manner by considering two independent sinusoidal variations in both  $x$  and  $y$  directions, parallel and perpendicular to the extensional axis of the sample. The general form of this director field is

$$\beta(\mathbf{r}) = C_x \sin(x/a) + C_y \sin(y/b) \quad (3)$$

where  $C_x$  and  $C_y$ , and  $a$  and  $b$  represent the amplitudes and the periods of orthogonal sinusoidal variations. The calculations indicate that parameters  $C_x$  and  $C_y$  control the intensity of the reflections, and  $a$  and  $b$  the positions



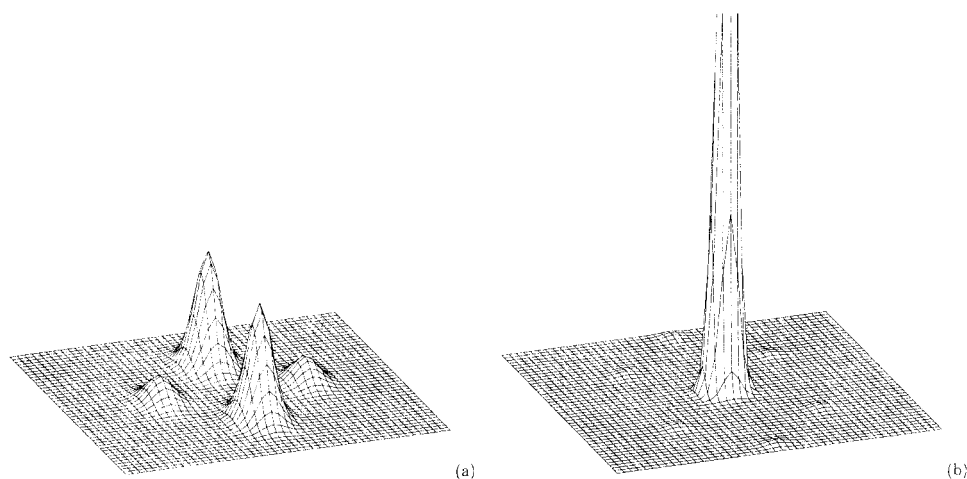


**Figure 8.** Calculated scattering pattern in the (a)  $HV_0$  and (b)  $HV_{45}$  configurations for the two-dimensional sinusoidal model discussed in the text. The model parameters  $C_x/C_y$ ,  $a = 4$  and  $b = 4$  were used.

of the corresponding orthogonal sets of reflections. The calculated scattering based on such a model with crossed polars oriented parallel to the extensional axis ( $HV_0$ ) and at  $45^\circ$  to it ( $HV_{45}$ ) is given in Figure 8. The modulation amplitudes used in calculating this pattern were  $C_x = 10^\circ$  and  $C_y = 20^\circ$ . Figure 8 illustrates that a simple model (eq 3) predicts four peaks in the  $HV_0$  configuration with two pairs of peaks with different intensities in good agreement with the experimental data of Figure 4a. On rotation of the polars with respect to the sample the peaks are calculated to fall in intensity, disappearing in the  $HV_{45}$  configuration, again in good agreement with the experimental data in Figure 4b. In the  $HV_{45}$  configuration, Figure 8b, the model predicts that other, second-order reflections appear, although significantly weaker (about 100 times) than the main peaks evident in the  $HV_0$  pattern. These additional peaks are too weak and cannot be observed in the experimental  $HV_{45}$  pattern. There is, however, some evidence for these very weak peaks in the experimental  $VV_0$  pattern, which can be shown to provide information similar to that from the  $HV_{45}$  pattern. The elongated nature of narrow peaks in the experimental pattern, in the direction perpendicular to the extension, suggests that a range of periodicities is present around the dominant  $d$  spacing. The broad peak, in the extensional direction, has a rounder shape, indicating a much more narrow distribution of characteristic spacing. (As the relative positions of the peaks are approximately equal and do not significantly alter with extension, the modulation periods  $a$  and  $b$  are taken to be equal and constant over the experimental conditions.)

An alternative model with an orthogonal director modulation consisting of a product of the form  $\beta = C \sin(x/a) \sin(y/b)$ , which has been known to describe a number of two-dimensional textures in liquid crystals,<sup>33</sup> could not reproduce the experimental patterns successfully.

On the basis of the model in eq 3, the relative values of modulation amplitudes  $C_x/C_y$  can be obtained from the experimental scattering patterns as a function of extension. Calculations suggest that values of  $C_x$  and  $C_y$  must be smaller than about  $35^\circ$  to recreate the correct form of the experimental patterns. The experimentally determined relative intensities of the narrow and broad peaks, typically 6:1, indicate that  $C_x/C_y =$

0.3–0.6 where  $C_x$  in the extensional direction is smaller than  $C_y$  in the perpendicular direction. This result indicates that oscillations of the mesogens in the extensional direction are more damped than those normal to it.

Although we cannot investigate the texture of the sample at zero stress because of poor transmission, it is clear that on increasing the extension the director texture that gives rise to the peaks in the scattering patterns is increasingly lost, suggesting that these peaks arise from the remnants of the low strain director texture characterized by a high-amplitude variations of the angle  $\beta$ . The real space image under crossed polars that this two-dimensional sinusoidal divergence function model would produce is presented in Figure 3b. It exhibits a texture very similar to that sketched in Figure 3a. The optical microscope image of the sample when illuminated with white light is colored. This coloring is similar to that observed when a sensitive tint plate is used to determine the sign of the birefringence of a polymer spherulite.<sup>14</sup> The colors arise from destructive interference of one wavelength of light leaving the complementary Newton colors. The colors depend on the orientation of the birefringent elements under the polars. These considerations can explain the colors in the image of our sample where the mesogens sinusoidally fluctuate along the  $x$  and  $y$  directions. The combination of the two modulations gives rise to the color scheme experimentally observed. The calculated real space image, colored to reflect this effect, is in good agreement with the experimental image.

**4.3. Intensity at  $q = 0$ .** Although this model of additive two-dimensional director modulations shows the correct form of variation in peak intensity with rotation of the sample, the magnitude of the experimentally measured scattering at zero scattering angle in the  $HV_{45}$  configuration is significantly larger than that calculated from the model when considered relative to the intensity of peaks in the  $HV_0$  pattern. This suggests that there are additional regions in the sample with the director well-aligned in the extensional direction, not participating in the orthogonal director modulation described by eq 2. These would not contribute to the  $HV_0$  pattern at all but would give an increased intensity in the  $HV_{45}$  configuration. The intensity of the scattering at  $q = 0$  increases with extension as the

director in all domains becomes more aligned in the extensional direction.

The high degree of orientational alignment of  $\mathbf{n}(\mathbf{r})$  at high strain/stress that gives the intense light scattering at  $q = 0$  is reflected in the X-ray scattering patterns, Figure 7a, and the mean orientation parameter  $S$  calculated from them. The  $HV_{45}$  light scattering also reflects this increased alignment, as well as indicating a continuing gradual increase in alignment with strain above the plateau stress.

## 5. Conclusions

The simple model used here to interpret the light and X-ray scattering and real space images does not include other features that may also be present and of particular theoretical interest, such as the presence of domain walls between the "domains". The size of domain walls, if they still remain in the stretched sample, can be estimated from the real space images as less than 0.5  $\mu\text{m}$ . Theoretical analysis predicts them to be even thinner,  $\sim 10^{-7}$  m,<sup>13,34</sup> well beyond the range of optical microscopy and light scattering measurements.

We conclude that the morphology of nematic elastomers undergoing a P–M transition, suggested by the results presented here, is that of periodic modulation of the director field at low strains. This modulation has been characterized by simple two-dimensional sinusoidal functions, although more complex periodic functions may also be consistent with the experimental scattering. Under stress, the director in all domains is increasingly reoriented into the extensional direction, without a noticeable change of period, contrary to an expectation that the domain sizes would change in a coarsening texture.

The alignment of mesogens under extension is reflected in the loss of the peaks in the  $HV_0$  pattern and the increase in intensity in the  $HV_{45}$  pattern. We conclude that the portion of initial domains that were already aligned close to the extensional direction continues to improve their orientation, contributing to the  $HV_{45}$  scattering. In contrast, the domains that were at large angles ( $\sim \pi/2$ ) to this direction are forced to reorient via periodic patterns of director orientations. Such an effect, very similar to the stripe domains,<sup>3,34</sup> is likely to be caused by the elastic constraints on the shape of approximately uniform nematic domains undergoing a director rotation, surrounded by other domains imposing an incompatible set of deformations. Since the local director rotation in each "domain" causes the corresponding local shear deformation in the elastic network, the overall mechanical constraint on the sample shape demands that the integral shear (and hence the integral sense of director rotation) must vanish; the present study shows that this global cancellation occurs in a periodic fashion, as eq 3 suggests.

To summarize, a combination of light scattering, optical microscopy, and X-ray scattering have been used to investigate the morphology of a polydomain nematic elastomer and the changes that occur in it under extension and on variation of temperature. At low extensions, the polydomain materials are opaque and cannot be investigated directly by optical techniques. However, as the materials first become transparent with extension, scattering from remnants of the texture in the low strain region can be investigated. The experimental data have been interpreted as an additive two-dimensional sinusoidal variation of the director field.

**Acknowledgment.** We appreciate valuable discussions with M. Warner, P. L. Taylor, and S. V. Fridrikh. Special thanks to Dr. M. Vickers of the Department of Material Science in Cambridge for the use of the X-ray facilities. This work has been supported by the EPSRC UK (S.C.M. and E.M.T.) and by the Deutsche Forschungsgemeinschaft and Fonds der Chemischen Industrie, Germany (I.K. and H.F.).

## Appendix: Scattering Amplitude in the RDG and AD Approximations

The interpretation of scattering by birefringent samples in the RDG approximation has been extensively discussed previously.<sup>15</sup> As a first approximation, we model the local director as varying only in a plane. The form of the amplitude of scattering when confining the axis of birefringence to the plane of the sample is described in ref 15 where  $\phi$ , as defined by them as the angle of the director with respect to the sample plane, is taken to be zero. Under these conditions the scattering amplitude takes the form of  $A_{HV}$  for scattering under crossed polars and the form of  $A_{VV}$  for scattering under parallel polars, eq 2 presented in the Introduction. These equations have also been derived by other authors.<sup>14,27</sup>

The anomalous diffraction approximation for birefringent material has been described by Meeten.<sup>16,17</sup> For a scattering object that is only two-dimensional the only variation across the sample is the orientation of the mesogens parametrized by a single angle  $\beta(\mathbf{r})$ . The Jones matrix is given for each element is given by

$$\mathbf{K}(\mathbf{r}) = \begin{bmatrix} e^{i\Phi_e} & 0 \\ 0 & e^{i\Phi_o} \end{bmatrix} \quad (4)$$

where  $\Phi_e$  and  $\Phi_o$  are the (constant) phase differences for the extraordinary and ordinary rays through the sample at that point, which are related to the local refractive indices of the medium,  $m_{||}$  and  $m_{\perp}$ , and that of the surroundings,  $m_s$ :

$$\Phi_e = kD \frac{m_e - m_s}{m_s}; \quad \Phi_o = kD \frac{m_o - m_s}{m_s} \quad (5)$$

In these expressions  $k$  is the wave vector of light,  $2\pi/\lambda$ , and  $D$  is the (constant) sample thickness. Ordinary and extraordinary refractive indices  $m_o$  and  $m_e$  are the  $m_{||}$  and  $m_{\perp}$  of the birefringent nematic, or vice versa, depending on the molecular electronic details. In our case, for a disordered liquid crystalline system, the refractive index of the surrounding is the average  $m_s = 1/3[m_{||} + 2m_{\perp}]$ .

The orientation of the local optical axis is included with the appropriate rotational transformations  $\mathbf{K}' = \mathbf{Q} \cdot \mathbf{K} \cdot \mathbf{O}^T$ , where  $\mathbf{O}$  is given by

$$\mathbf{O} = \begin{bmatrix} \cos(\phi - \beta) & \sin(\phi - \beta) \\ -\sin(\phi - \beta) & \cos(\phi - \beta) \end{bmatrix} \quad (6)$$

and the angle  $\beta(\mathbf{r})$  describes the orientation of the local director. For an incident beam polarized along the  $x$  direction and scattering geometry as given in Figure 9:

$$\begin{pmatrix} E_{r0} \\ E_{r0} \end{pmatrix} = \begin{bmatrix} \cos \phi & \sin \phi \\ \sin \phi & -\cos \phi \end{bmatrix} \begin{pmatrix} E_0 \\ 0 \end{pmatrix} \quad (7)$$

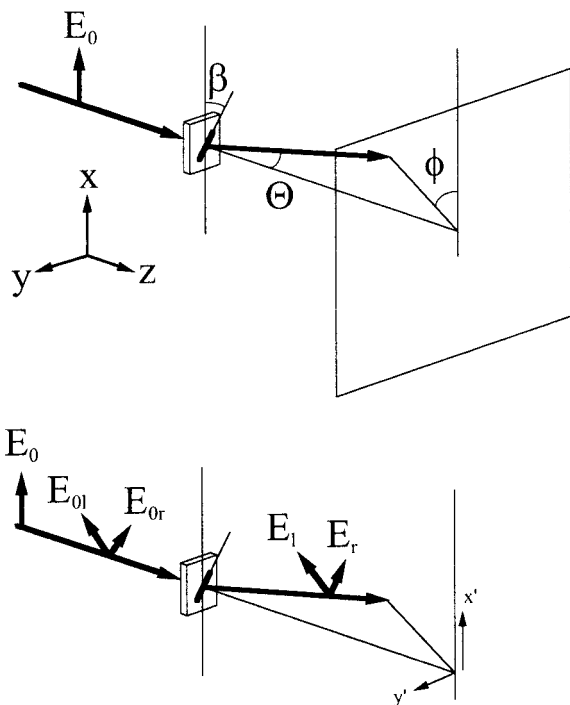


**Figure 9.** Diagram of the optical geometry, indicating the plane of polarization of the incident light,  $E_0$ , the electric vectors in the scattering plane,  $E_0$ ,  $E_{r0}$ ,  $E_i$ , and  $E_r$ , and the local director orientation,  $\beta$ , with respect to the plane of polarization of the incident light.

The scattering matrix  $\mathbf{S}$ , as defined by Van de Hulst,<sup>35</sup> relates the electric vectors before and after scattering,  $E_{0,r0}$  and  $E_{i,r}$ :

$$\begin{pmatrix} E_i \\ E_r \end{pmatrix} = \frac{1}{ikr_0} e^{-ikr_0} \begin{bmatrix} S_2 & S_3 \\ S_4 & S_1 \end{bmatrix} \begin{pmatrix} E_{i0} \\ E_{r0} \end{pmatrix} \quad (8)$$

$r_0$  is the distance from the sample to the detector. Meeten has proposed that the matrixes  $\mathbf{S}$  and  $\mathbf{K}$  are related by

$$\mathbf{S} = \frac{k^2}{2\pi} \int dx' dy' e^{-ikr'} [(\cos \theta) \delta - \mathbf{K}']$$

where the integrals are over the area of the sample. For each element of the sample we can write, per unit area

$$\begin{bmatrix} S_2 & S_3 \\ S_4 & S_1 \end{bmatrix} = \frac{k^2}{2\pi} e^{-ikr'} \begin{bmatrix} (1 - K_2) \cos \theta & -K_3 \cos \theta \\ -K_4 & (1 - K_1) \end{bmatrix} \quad (9)$$

The scattering amplitude from each element under crossed,  $A_{HV}$ , or parallel,  $A_{VV}$ , polars is now calculated by rotating the scattered electric vector ( $E_i$ ,  $E_r$ ) into the laboratory frame based on the axes of polarizer ( $x'$ ,  $y'$ ). For small scattering angle  $\theta$  the scattering amplitude in the  $x', y'$  plane is

$$\begin{pmatrix} E_{x'} \\ E_{y'} \end{pmatrix} = \begin{bmatrix} \cos \phi & \sin \phi \\ \sin \phi & -\cos \phi \end{bmatrix} \begin{pmatrix} E_i \\ E_r \end{pmatrix} \quad (10)$$

to second order in  $\theta$  and  $\phi$ , and for an ideal polarizer.<sup>16</sup>

Performing the matrix manipulations, we obtain the scattering amplitudes  $A_{HV} = E_{y'}/E_0$  and  $A_{VV} = E_{x'}/E_0$  for small angle scattering, per unit area of the sample:

$$A_{HV} = -\frac{ik}{4\pi r_0} e^{-i(\Phi_e + \Phi_0)} (e^{i\Phi_e} - e^{i\Phi_0}) \sin 2\beta \quad (11)$$

$$A_{VV} = -\frac{ik}{2\pi r_0} e^{-i(\Phi_e + \Phi_0)} (-e^{i\Phi_e} \sin^2 \beta + e^{i(\Phi_e + \Phi_0)} - e^{i\Phi_0} \cos^2 \beta) \quad (12)$$

Note that the form of the scattering amplitudes, eq 2, is recovered in this calculation under the AD approximation. Under the additional approximation of very small birefringence,  $\Phi_{e,0} \ll 1$ , we obtain the particularly simple equations, almost exactly equal to the RDG approximation results:

$$A_{HV} \approx \frac{k^2 D}{4\pi r_0} \frac{m_e - m_0}{m_s} \sin 2\beta;$$

$$A_{VV} \approx \frac{k^2 D}{2\pi r_0} \left( \frac{m_0 - m_s}{m_s} + \frac{m_e - m_0}{m_s} \cos^2 \beta \right) \quad (13)$$

This useful result allows the straightforward calculation of the scattering patterns from the model director distributions given by  $\beta(\mathbf{r})$ .

## References and Notes

- (1) Warner, M.; Terentjev, E. M. *Prog. Polym. Sci.* **1996**, *21*, 853.
- (2) Barclay, G. G.; Ober, C. K. *Prog. Polym. Sci.* **1993**, *18*, 899.
- (3) Kundler, I.; Finkelmann, H. *Macromol. Rapid Commun.* **1995**, *16*, 679.
- (4) Nishikawa, E.; Finkelmann, H.; Brand, H. R. *Macromol. Rapid Commun.* **1997**, *18*, 65.
- (5) Davies, F. J.; Mitchell, G. R. *Polym. Commun.* **1987**, *28*, 8.
- (6) Schatzle, J.; Finkelmann, H. *Makromol. Chem.* **1989**, *190*, 3269.
- (7) Kupfer, J.; Finkelmann, H. *Macromol. Chem. Phys.* **1994**, *195*, 1353.
- (8) Hunter R. J. *Foundations of Colloid Science*; Oxford University Press: Oxford, U.K., 1989; Vol. II.
- (9) Hashimoto, T.; Nakai, A.; Shiwaiku, T.; Hasegawa, H.; Rojstaczer, S.; Stein, R. S. *Macromolecules* **1989**, *22*, 422.
- (10) Deutsch, M. *Phys. Rev. A* **1991**, *44*, 8264.
- (11) Leadbetter, A. J.; Norris, E. K. *Mol. Phys.* **1979**, *38*, 669.
- (12) Kohli, M.; Otnes, K.; Pynn, R.; Riste, T. *Z. Phys. B* **1976**, *24*, 147.
- (13) Fridrikh, S. V.; Terentjev, E. M. *Phys. Rev. Lett.* **1997**, *79*, 4661.
- (14) Haudin, J. M. In *Optical Properties of Polymers*; Meeten, G. H., Ed.; Elsevier Applied Science: London, 1986.
- (15) Rhodes, M. B.; Stein, R. S. *J. Polym. Sci., A-2* **1969**, *7*, 1539.
- (16) Meeten, G. H. *Opt. Acta* **1982**, *29*, 759.
- (17) Champion, J. V.; Killey, A.; Meeten, G. H. *J. Polym. Sci., Polym. Phys. Ed.* **1985**, *23*, 1467.
- (18) Clarke, S. M.; Nishikawa, E.; Finkelmann, H.; Terentjev, E. M. *Macromol. Chem. Phys.* **1997**, *198*, 3485.
- (19) Clarke, S. M.; Ottewill, R. H.; Rennie, A. R. *Adv. Colloid Interface Sci.* **1995**, *60*, 95.
- (20) Clarke, S. M.; Rennie, A. R. *Faraday Discuss.* **1996**, *104*, 49.
- (21) Polaroid material HN22 from COMAR Instruments, Cambridge, U.K.; stress gauge and controller, models UF1 and AD20P, from Pioden Controls Ltd., U.K.; Thermostatic controller Cal3200, from Cal Controls Ltd., U.K.
- (22) Butler, M. F.; Donald, A. M.; Bras, W.; Mant, G.; Derbyshire, G. E.; Ryan, A. J. *Macromolecules* **1995**, *28*, 6383.
- (23) Zubarev, E. R.; Talroze, R. V.; Platé, N. A.; Finkelmann, H. *Macromolecules*, to be published; *Macromol. Chem. Phys.* **1997**, *198*, 2121.
- (24) Ortiz, C.; Ober, C. K.; Kramer, E. J. *J. Mater. Sci.*, to be published.
- (25) Clough, S.; van Aartsen, J. J.; Stein, R. S. *J. Appl. Phys.* **1963**, *36*, 3072.
- (26) Samuels, R. J. *J. Polym. Sci., A-2* **1969**, *7*, 1197.

- (27) Viney, C.; Windle, A. H. *Polymer* **1986**, 27, 1325.
- (28) Stein, R. S. *Pure Appl. Chem.* **1991**, 63, 941.
- (29) Stein, R. S.; Wilson, P. R. *J. Appl. Phys.* **1962**, 33, 1914.
- (30) Donald, A. M.; Viney, C.; Windle, A. H. *Polymer* **1983**, 24, 155.
- (31) Viney, C.; Donald, A. M.; Windle, A. H. *J. Mater. Sci.* **1983**, 18, 1136.
- (32) Born, M.; Wolf, E. *Principles of Optics*; Pergamon Press: Oxford, U.K., 1970.
- (33) Lowe, M.; Golub, J. P.; Lubensky, T. C. *Phys. Rev. Lett.* **1983**, 51, 786. Terentjev, E. M.; Pikin, S. A. *Sov. Phys. Crystallogr.* **1987**, 32, 1001.
- (34) Verwey, G. C.; Warner, M.; Terentjev, E. M. *J. Phys. II* **1996**, 6, 1273.
- (35) Van der Hulst, H. C. *Light Scattering by Small Particles*; Dover: London, 1981.  
MA980195J